Mitochondrially Transcribed dsRNA Mediates Manganese-induced Neuroinflammation.

Avanti Gokhale[1*], Hadassah Mendez-Vazquez[1*], Maureen M. Sampson[2], Felix G Rivera Moctezuma[7], Adriana Harbuzariu[3], Anson Sing[2], Stephanie A. Zlatic[1], Anne M. Roberts[4,5], Milankumar Prajapati[6], Blaine R. Roberts[4,5], Thomas B. Bartnikas[6], Levi B. Wood[7,8], Steven A. Sloan[2], Victor Faundez[1], Erica Werner[1#]

[*]These authors contributed equally

[#]Corresponding author

[1]Department of Cell Biology, Emory University, 615 Michael St, Atlanta, GA, USA, 30322

[2]Department of Human Genetics, Emory University, 615 Michael St, Atlanta, GA, USA, 30322

[3]Emory Stem Cell and Organoids Core, Emory University, 615 Michael St, Atlanta, GA, USA, 30322

[4]Department of Biochemistry, Emory University, 1510 Clifton Rd, Atlanta, Georgia, USA, 30322

[5]Department of Neurology, Emory University, 12 Executive Park Dr NE, Atlanta, Georgia, USA, 30322

[6] Department of Pathology and Laboratory Medicine, Brown University, Providence, RI, 02912, USA.

[7]George W. Woodruff School of Mechanical Engineering and Parker H. Petit Institute for Bioengineering and Bioscience, Georgia Institute of Technology, 315 Ferst Dr, Atlanta, GA 30332

[8]Wallace H Coulter Department of Biomedical Engineering, Georgia Institute of Technology, 315 Ferst Dr, Atlanta, GA 30332

Corresponding author email: Erica Werner, ewerner@emory.edu

Key words: dsRNA, manganese, astrocyte, interferon

Major classification: Biological Sciences

Minor classification: Neuorscience

Acknowledgements:
This work was supported by NIH grant R01ES034796 to AG and EW, Udall Center Pilot Project Grants for Parkinson's Disease Research to AG, Hercules Pilot Grant to EW and AG, NIH T32NS096050 to HM-V, NIH K00 ES033033 and BWF PDEP to MMS, NIMH R01 MH125956 to SAS, 1R01AG075820 to LBW, FGRM was funded in part by the Cell and Tissue Engineering Training Grant NIH T32GM145735 NIGMS, NIH R01 DK110049 to TBB. Research reported in this publication was supported in part by Emory University subsidized cores: Emory Integrated Genomics Core (EIGC, RRID# iSCR_023529), Emory Multiplexed Immunoassay Core (EMIC), Emory Stem Cell and Organoids Core (ESCOC RRID# SCR_023264), Integrated Cellular Imaging (ICI, RRID:SCR_023534) of the Winship Cancer Institute of Emory University and NIH/NCI under award number, 2P30CA138292-04.

Abstract

Manganese (Mn) is an essential trace element required for various biological functions, but excessive Mn levels are neurotoxic and lead to significant health concerns. The mechanisms underlying Mn-induced neurotoxicity remain poorly understood. Neuropathological studies of affected brain regions reveal astrogliosis, and neuronal loss, along with evidence of neuroinflammation. Here, we present a novel Mn-dependent mechanism linking mitochondrial dysfunction to neuroinflammation. We found that Mn disrupts mitochondrial transcriptome processing, resulting in the accumulation of complementary RNAs that form double-stranded RNA (dsRNA). This dsRNA is released to the cytoplasm, where it activates cytosolic sensor pathways, triggering type I interferon responses and inflammatory cytokine production. This mechanism is present in 100-day human cerebral organoids, where Mn-induced inflammatory responses are observed predominantly in mature astrocytes. Similar effects were observed in vivo in a mouse model carrying mutations in the SLC30A10 gene, which results in Mn accumulation. These findings highlight a previously unrecognized role for mitochondrial dsRNA in Mn-induced neuroinflammation and provide insights into the molecular basis of manganism. We propose that this mitochondrial dsRNA-induced inflammatory pathway has broad implications in for neurodegenerative diseases caused by environmental or genetic insults.

Introduction:

Manganese is an essential metal for living organisms at trace levels, however its excess is neurotoxic (1). Toxic manganese accumulation occurs as a result of environmental factors, genetic defects, and/or secondary to liver damage (2). Environmental exposures occur from contaminated water, air, and soil affecting broader populations or occupationally in miners, welders, and industrial workers (3-5). Increased manganese levels in organs and the brain can also occur as a result of genetic defects in manganese transporters controlling manganese influx (SLC39A14) or efflux (SL30A10) from cells and organisms (6-8).

The brain is one of the most sensitive organs to excess manganese exposure by genetic or environmental routes. In the brain, manganese accumulates predominantly in the basal ganglia causing manganism, a condition characterized by early neuropsychiatric symptoms, progressive dystonia and extrapyramidal dysfunction (9, 10). Exposure to manganese at chronic low levels also increases the risk of cognitive, neuropsychiatric and behavioral symptoms in young and at-risk adult individuals (5, 11).

The mechanisms for manganese brain toxicity remain poorly understood. Neuropathological studies of the globus pallidus in non-symptomatic and symptomatic individuals following manganese exposures, showed astrogliosis, elevated glia counts and neuronal loss (12-15). Cytokines produced by microglia and astrocytes can be detected at early and late stages of disease and in brains of manganese exposed mice, indicating a neuroinflammatory component to the pathogenic mechanism of toxicity in the brain (16-20). Both microglia and astrocytes respond to manganese with cytokine production (21), and these responses can interact and synergize in vitro as demonstrated by co-culture experiments showing that microglia factors released after manganese treatment modulate the responses in astrocytes. For example, TNFα produced by microglia in response to manganese mediated increases in IL -1β and Ccl2 but not of IL6 and Ccl5 in astrocytes (22). Similarly, Manganese-induced inflammatory responses on glial cells exacerbate the metal toxicity in neurons (23, 24). Neuroinflammation is a response to injury, common to many neurodegenerative diseases that is proposed to be involved in both, disease initiation and progression (25, 26). While induction mechanisms for neuroinflammation have been proposed to be disease-specific, in manganism, the mechanisms underlying neuroinflammatory upregulation remain largely unknown. Here, we present a novel manganese-dependent mechanism for the induction of neuroinflammation that requires the generation of double stranded RNA (dsRNA) in mitochondria.

We previously found that manganese disrupts processing of the mitochondrial transcriptome and induces accumulation of un-processed mitochondrial transcripts intermediaries

(27). Processing of the mitochondrial polycistronic RNA is necessary to generate functional ribosomal, transfer, and messenger RNAs, which are required to synthetize the thirteen mitochondrial-encoded proteins necessary for the assembly and function of the respiratory chain (28). The bidirectional transcription of the mitochondrial DNA generates long complementary RNA which are homeostatically maintained by mitochondrial specific post-transcriptional modifications and degradation of non-coding transcripts (29, 30). Accumulation of complementary RNA has the potential to generate mitochondrial dsRNA, which can translocate to the cytoplasm, be recognized by cytosolic sensor molecules and trigger antiviral signaling pathways to produce type I interferon (IFN) responses and inflammation (31-33). We tested the hypothesis that processing defects of the mitochondrial transcriptome caused by manganese are sufficient to induce inflammatory signaling. Here, we demonstrate that at sub-cytotoxic doses, manganese induces dsRNA accumulation in mitochondria, which triggers the IFN type I response as well as the production of inflammatory cytokines in cell lines and in the most mature subpopulation of astrocytes in 100-day old human cerebral organoids. The in vitro neural tissue inflammatory responses are reproduced in vivo by the mouse brain of a genetic model of manganese accumulation due to mutation of the *Slc30a10* gene (34, 35).

Results

Exposure to manganese leads to the accumulation of mitochondrial dsRNA

We previously found that manganese alters mitochondrial RNA processing, measured by molecular counting employing a custom NanoString panel designed to detect mitochondrial mRNA, tRNA-mRNA, and tRNA-rRNA junctions as well as non-coding regions in both, H and L strand transcripts (27, 36). On close analysis, we observed the accumulation of L strand non-coding RNA sequences, which are normally degraded (30, 31), accumulated in Hap1 SLC30A10^{KO}cells as well as HAP1 and HeLa cells treated for 24h with manganese at 150 and 800μM respectively (Fig. 1A). In contrast, transcripts levels for TFAM, SDHA, or POLMRT did not change consistently, indicating no change in mitochondrial mass. Linear and non-linear dimensionality reduction of the data by principal component analysis and by Uniform Manifold Approximation and Projection (UMAP), demonstrated clustering of all the control samples and segregating away from all samples with increased manganese resulting from either manganese exposure or mutagenesis of the SLC30A10 efflux transporter (Fig. 1B). The alterations of the mitochondrial transcriptome after manganese exposure of wild-type cells occur at IC_{50} metal doses (50% death when survival was measured at day 3 post-metal treatment, Fig. 3E and S1C (27)). These manganese doses elicited comparable increases in intracellular manganese levels in both cell lines, without affecting Zn^{2+} or Ca^{2+} (Fig. 1C).

We reasoned that the dysregulated persistence of RNA transcripts of complementary sequence belonging to the H and L-strands could lead to dsRNA accumulation in mitochondria. We tested this hypothesis by detecting dsRNA co-localization with the mitochondrial RNA granule component GRSF1 by immunofluorescence with the J2 antibody, a monoclonal antibody that binds to dsRNA molecules larger than 40bp irrespective of sequence (37) (Fig. 1D). Both cell lines showed increased levels of dsRNA in mitochondria following 24h manganese treatment. dsRNA immunoreactivity was downregulated by inhibition of the mitochondrial RNA polymerase POLRMT with IMT1 (38), indicating the mitochondrial origin of the dsRNA signal induced by manganese is mitochondrial transcription (Fig. 1E). We confirmed that the J2 antibody selectively recognized dsRNA by degrading dsRNA specifically with RNAse III before immune labeling (Fig. 1E).

Manganese induced dsRNA activate type I Interferon responses

dsRNA of mitochondrial origin are known to escape from mitochondria into the cytoplasm where they are recognized by the dsRNA receptors, retinoic acid inducible gene 1 (RIG-1) and melanoma differentiation-associated protein 5 (MDA5), reviewed in (32). Once bound to dsRNA, these receptors are then recruited to a multiprotein aggregate comprised of MAVS and signaling

proteins. This multiprotein assembly activates the kinase TBK1, which phosphorylates IRF3, enabling its nuclear translocation to induce IFNβ transcription. The produced IFNβ activates a cascade of interferon-stimulated genes (ISGs) (32, 39) (Fig. 2A). To test the activation of this dsRNA receptor pathway by manganese, we expressed a reporter construct in which the IFNβ promoter drives luciferase expression. While HAP1 cells accumulated significant levels of dsRNA in mitochondria (Fig. 1D, E), no manganese concentration induced luciferase expression in these cells (Fig. 2B). This outcome suggests that dsRNA is retained in mitochondria in HAP1 cells, because the pathway was readily triggered by delivery of the membrane-permeable synthetic dsRNA agonist, poly(I:C) (Fig. 2B). In contrast, sub-IC_{50} manganese doses were sufficient to increase luciferase activity up to four-fold in HeLa cells (Fig. 2B). We next identified the receptor that recognizes manganese-induced mitochondrial dsRNA in the cytosol by knockdown experiments. Reduced expression of MDA5, but not RIG1, downregulated manganese-induced luciferase activity by 40% (± 11% SEM) (Fig. 2C). Combination knockdown of RIG1 and MDA5 did not change the inhibitory effect of MDA5 downregulation, indicating that of the two dsRNA receptors, only MDA5 is required for recognizing manganese-induced dsRNA. In contrast, RIG1 was the receptor for poly(I:C) (Fig. 2C). We further confirmed mitochondrial dsRNA signaling by pharmacological inhibition of predicted components in the pathway (Fig. 2A, 2D). Interferon promoter transcription was reduced by downregulating mitochondrial transcription with the inhibitor IMT1, which targets the mitochondrial RNA polymerase (POLRMT). Interferon promoter transcription was also reduced by interfering with dsRNA export to the cytosol by either inhibiting the permeability transition pore function in the inner mitochondrial membrane with cyclosporine A (CspA) or by blocking the Bax-Bak mitochondrial pore in the outer mitochondrial membrane with V5 peptide (40-43) (Fig. 2A). None of these inhibitors reduced manganese uptake by cells (Fig. 2D top panel) but all reduced IFNβ transcription by at least 25%, with 100% decrease when TBK1 was inhibited with GSK8612 (Fig. 2D bottom panel). Another potent activator of the antiviral pathway is the release of mitochondrial DNA (mtDNA) into the cytosol which activates the cGAS-STING converging to TBK-1 activation (Fig. 2A). We excluded a contribution of mtDNA to signaling by pharmacological inhibition of STING with H151, which did not affect manganese or poly(I:C) induced luciferase transcription (Fig. 2E). H151 successfully blocked STING activation-induced transcription by the agonist 2'3 c-di-AM$(PS)_2$ Rp,Rp (ADU S100) (Fig. 2E). Taken together, these results indicate that manganese increases dsRNA in mitochondria of both cell lines, but dsRNA reach the cytoplasm where they bind to MDA5 and lead to increased IFNβ transcription only in HeLa cells.

Manganese-induced accumulation of mitochondrial dsRNA results in neuroinflammatory responses

Next, we asked whether IFN activation occurs in the context of a broader inflammatory response by profiling conditioned media of HAP1 and HeLa cells following a 48h manganese exposure with a cytokine profiling antibody array (Fig. 3A). While no significant changes were detected in HAP1 cells (Fig. S1B), we identified several cytokines and chemokines induced in response to increased manganese concentration in HeLa cells (Figs. 3A, 3B, S1A). Notably, the chemokines CXCL10 and GM-CSF were robustly upregulated by manganese, both of which have been shown to be upregulated following poly (I:C) treatment of epithelial cells (44). We detected modest increases in IL8, but not IL6, in the cytokine array which we confirmed by ELISA assay (Fig. 3C, 3D). We focused on IL8 production to monitor manganese-induced inflammatory responses as this cytokine is responsive to both interferon and NFκB activation by indirect and direct mechanisms, respectively and all cell types in the brain express receptors for this chemokine (45).

Manganese induced IL8 expression following 48h treatment with a sub-IC_{50} manganese dose (Fig. 3C, 3E). This upregulation was reduced by inhibition of the mitochondrial RNA polymerase POLRMT with IMT1, the Bax-Bak pore function with V5 peptide, or a TBK1 inhibitor (Fig 3D). Importantly, none of the inhibitors affected cell survival of either cell line in response to manganese, which suggests that the inflammatory responses induced by dsRNA do not play a role in cytotoxicity (Fig. 3E, S1C). Addition of the pan-caspase inhibitor Q-VD-Oph reduced cytotoxicity in HAP1 cells (Fig. S1C) but did not affect HeLa survival, indicating that no apoptotic mechanisms play a role in this inflammatory response either (Fig. 3E, S1C).

To gain further understanding of how manganese cytotoxicity and inflammation take place in a model system for brain tissue, we studied the effects of manganese on the mitochondrial transcriptome and cytokine secretion in human hiPSC-derived cerebral organoids. We chose the unguided method for organoid growth as it provides diversified cell types and developmental paths to interrogate (46, 47). To select the appropriate developmental timepoint to analyze, we tested for processing of mitochondrial transcripts over organoid development with the MitoString panel, which we customized by adding probes to quantify differentiation of neuroprogenitor cells (NPC), neurons, and astrocytes. We found that neuroprogenitor cell markers declined overtime from Day 30 on, with a steady increase in neuron maturation and astrocyte markers at Days 60 and 100 (Fig 4A, 4B). These transcriptional differentiation responses occurred concomitantly with morphological maturation and layering of the organoids as determined by confocal

immunomicroscopyμ with antibodies against the cortical layer markers Ctip2 and Satb2 and by the progressive loss of immunoreactivity of the neuroprogenitor marker Sox2 (Fig. S2A).

The organoids were treated with manganese for 48h at several times of their development. After treatment organoids were collected for RNA analysis and conditioned media for cytokine measurement. We used a dose of 250μM manganese, a concentration that is approximately equivalent to the metal concentrations estimated to accumulate in the striatum and globus pallidus of manganese-exposed primate and rodent models (48). Using this strategy, we found that 30- and 60-day organoids did not show significant changes in mitochondrial-encoded RNAs or levels of their processing intermediaries. However, we found robust changes in 100-day organoids, including increases of most of the mitochondrial-encoded mRNA, some tRNA-mRNA junctions and several non-coding RNA encoded in the L strand of the mitochondrial genome (Fig. 4C). These modifications of the mitochondrial transcriptome occurred without changes in the nuclear-encoded mitochondrial genes TFAM, POLG, and POLRMT, excluding increases in mitochondrial content in 100-day organoids after 48h of manganese exposure.

We comprehensively interrogated the bulk 100-day organoid transcriptome to characterize the identity of inflammatory responses induced by manganese employing the Neuroinflammatory (Fig.4D,4E) and Neuropathology (Fig. S2B, 2C) panels from NanoString. Hybridization with the Neuroinflammatory panel demonstrated upregulation of multiple inflammation-annotated mRNAs as represented in a volcano plot (Fig. 4D). Several genes that are transcriptional targets of IRF3 and NFκB as well as interferon stimulated genes (ISG) were significantly upregulated after manganese exposure (Fig. 4E). We measured secretion of inflammatory cytokines by analyzing the presence of IL6 and IL8 in conditioned organoid media with Mesoscale ELISA assays. Manganese significantly increased IL8 levels in conditioned media of organoids exposed to 250μM dose in two independent organoid cohorts (Fig. 4F, S2D). We observed a fraction of organoids with higher levels of basal cytokine secretion in the absence of manganese treatment (Fig. 4F, S2D). Basal untreated and manganese-induced cytokine secretion levels remained unaltered after normalizing organelle secretory activity and size by beta-2 microglobulin, a protein constitutively expressed and secreted by all cells (Fig. 4F). Analysis of the Neuropathology panel demonstrated that at this time of development and manganese concentration, there were no changes in the expression of transcripts annotated to either neurons and astrocytes or associated with disease mechanisms such as hypoxia, the unfolded protein response, or NRF2-dependent pathway signaling (Fig. S2C). Taken together, these results indicate that the manganese-induced mitochondrial and interferon type 1 inflammatory responses are present in brain cell types and are not part of an overt stress or cytotoxic response in brain organoids. Additionally, because

cerebral organoids lack microglia, these findings indicate that non-myeloid cells are competent to induce these inflammatory responses independent of microglial function.

Manganese induces neuroinflammation in astrocytes

To identify the cell types engaged in inflammatory responses to manganese in the organoids, we performed 10x scRNAseq on 12 individual organoids. Six organoids were left untreated and six were exposed to 250μM manganese for 48h. A total of 119,996 cells were analyzed and clustered into 8 distinct cell populations, including proliferative, fibroblast, choroid plexus, radial glia, astrocyte, neural progenitor, and two neuronal categories (Fig. 5A, QC metrics in Fig. S3A). All cell populations were proportionally present in all 12 organoids regardless of organoid size and Manganese treatment (Fig. 5B, S3C) or preferentially affected cell count in any specific cluster (Fig. S3D). Cell clusters were manually identified based on differential gene expression profiles (Fig. 5C) and were of restricted expression as demonstrated by Feature Plots (Fig. S3B). We also examined the expression of selected inflammatory genes and identified astrocytes as the major cell population driving inflammatory responses in the organoids following manganese treatment (Fig. 5C). To gain insights into the mechanisms and molecular phenotypes elicited by manganese treatment in astrocytes, we obtained the differentially expressed genes via pseudobulking and DESeq2 to compare control and treated organoids (Fig. 5D), then conducted gene ontology analysis (Fig. 5E). Significantly up- and down regulated genes are represented in a volcano plot, where we highlight genes relevant to astrocyte function, CXCL10 and selected genes annotated to the pathways identified in bioinformatic analysis (Fig. 5D). Transcripts upregulated by manganese were enriched in genes annotated to interferon alpha responses, cholesterol biosynthesis and oxidative phosphorylation pathways in the MSigDB Hallmark 2020 database (49). Downregulated transcripts were annotated to UV response, hypoxia and TGFβ signaling (Fig. 5E). These manganese-induced responses were elicited across the treated individual organoids (Fig. 5F). Manganese increased the expression of CXCL8 and CXCL10, mitochondrial genes, subunits of the respiratory chain, and interferon response genes. Genes induced by manganese correlated with higher mRNA levels of astrocytic reactivity markers, cholesterol synthesis, and neuron supporting genes, but lower levels of transcripts annotated to phagocytosis. Feature maps of CXCL8 and CXCL10 expression revealed that a subpopulation of astrocytes expressed these chemokines, suggesting heterogeneity among the astrocyte responses (Fig. 5G). To characterize and identify unique attributes of these chemokine-expressing astrocytes, we subclustered astrocytes into 3 sub-populations (Fig. 5H, Astro 1,2 and 3), where Astro 2 concentrated the cytokine expressing cells (Fig. 5I). Comparison of the differentially expressed genes in response to manganese showed that Astro 2 cluster also

concentrated cells with the most robust induction of the interferon response genes, accumulated mitochondrial-encoded transcripts, and displayed reduced expression of HSD17B10 and REXO2. HSD17B10 is a component of the mitochondrial RNA processing complex RNaseP (50) and REXO2 participates in mitochondrial dsRNA degradation (51) (Fig. 5I and Supplementary Dataset S8). This heterogeneity of astrocytic responses detected by scRNAseq was also evident by immunomicroscopy of manganese-treated organoids stained with antibodies against dsRNA and GFAP (Fig. 5J-1). We found that 36% of GFAP-positive astrocytes were also positive for dsRNA after exposing organoids to manganese (Fig 5J-2). Importantly, the dsRNA signal colocalized with mitochondrial markers in iPSC-derived astrocytes exposed to the same manganese challenge as organoids (Fig. 5J-3).

In vivo chronic increased manganese induces inflammation in brain and liver

While organoids are an in vitro model for brain tissue well-suited to perform dose- and time-controlled experiments of acute manganese exposures, we asked next whether inflammatory responses are part of the phenotype following chronic excess manganese accumulation in brain tissue in vivo. Mice with a global deficiency in the manganese efflux pump Slc30a10 progressively accumulate manganese in the brain from the diet (6). At eight weeks of postnatal age, *Slc30a10*$^{-/-}$ mice develop hypermanganesemia, reproducing several of the phenotypes observed in the human SLC30A10 genetic disease hypermanganesemia with dystonia 1 disorder (OMIM 613280) (6). We measured the expression levels of 32 cytokines in brain and liver samples from wild type and Slc30a10-/- mice of both sexes as we have done before (52). We included liver as this organ is one of the tissues with the highest levels of manganese in this mutant (6). We found a complex pattern of altered cytokine expression modulated by sex, with higher expression levels of cytokines in KO tissues in both organs (Figs. 6A and S4A). To resolve cytokines whose expression was strongly associated with the mutant genotype, we analyzed these data by discriminant partial least squares regression analysis, which enables us to study these multivariate datasets by reducing data from 32 measured variables to a reduced set of latent variables (LV1 and LV2) (Figs. 6B and S4B). Reducing the dataset to these latent variables allowed us to identify differences between genotypes distinguishing cytokine changes correlated with genotype from unrelated noise in the measurements (52-54). Each LV represents a profile of cytokines that vary together between wild type and KO animals. We found that LV1 distinguished wild type animals and KO animals, irrespective of sex (Figs. 6B and S4B, x axis). We used a leave-one-out cross validation strategy, wherein each animal was iteratively left out, and the discriminant partial least squares regression analysis was re-computed. We found low standard deviation in each cytokine, suggesting that the involvement of each cytokine is not

dependent on any single tissue sample (Figs. 6B and S4B). Moreover, the cytokine expression pattern was different in cortical and liver samples. For example, Vegf, a cytokine responsive to hypoxia was elevated in liver but not cortex of KO animals, reproducing previous RNAseq findings (55). In contrast, IL12b, was increased in both mutant tissues. (Figs. 6B and S4B). These results demonstrate a profile of inflammatory cytokines in several Slc30a10-/- tissues.

Discussion

We have identified a novel mechanism by which manganese induces inflammatory responses in non-immune cells, initiated by alterations in the processing of the mitochondrial-encoded transcriptome leading to activation of anti-viral type I interferon response in the cytoplasm and induction of inflammatory cytokines production. We show that manganese induces dsRNA accumulation localized to the mitochondrial RNA granule by immunofluorescence and the accumulation of unprocessed non-coding segments of mitochondrial transcripts in multiple cell types, including HeLa and HAP1 cells, and in astrocytes of cerebral organoids. We demonstrate the role of mitochondrial dsRNA in triggering pro-inflammatory signaling, employing pharmacological and genetic inhibition to interfere with signal transduction. IFNβ transcription and IL8 cytokine production can be downregulated by reducing mitochondrial transcription with the mitochondrial RNA polymerase inhibitor IMT1 or reducing dsRNA traffic from mitochondria to the cytosol with inhibitors targeting mitochondrial membrane permeability. We identified MDA5 as a dsRNA receptor in the cytoplasm signaling to the downstream kinase TBK1. The pharmacological inhibitors targeting early components of this pathway (upstream from TBK1 activation) and protein knockdowns, partially reduced the response at similar magnitude, in contrast with highly effective TBK1 inhibitors. This finding suggests that there may be additional manganese-induced mechanisms converging on TBK1 activation. One possible mechanism is potential binding of dsRNA to PKR in mitochondria, which then could contribute to signaling and TBK1 activation in the cytosol (56). Alternatively, manganese has been shown to increase ATM activity and modulate substrate specificity which leads to increased TBK1 activation (57, 58). Nevertheless, we found that TBK1 inhibitors were highly effective in downregulating interferon induction and interleukin 8 production, without affecting cell survival outcomes in HeLa cells. This finding indicates that mitochondrial permeability to dsRNA and downstream signaling is not a mechanism for manganese to induce cell death.

Cerebral organoids provided a model of concerted development for astrocytes and neurons to study manganese responses, in the absence of additional sources that may contribute to inflammation in vivo, such as microglia and blood vessels. We found that changes in mitochondrial RNA transcript processing and inflammatory responses emerged over time during organoid growth, coinciding with astrocyte development. Single cell RNAseq confirmed our findings with bulk RNA transcriptomes from organoids exposed to a short and non-lethal manganese treatment identifying the most mature astrocytes as the main cell type driving IL-8 and CXCl10 expression/secretion and the induction of interferon response genes. We confirmed by immunofluorescence that GFAP-positive cells accumulated dsRNA, suggesting that in this cell

population, manganese induces dsRNA and signaling to activate anti-viral responses and inflammation like the pathway induced in HeLa cells. Single cell RNAseq experiments have demonstrated large heterogeneity in astrocyte phenotypes across brain regions and in their capacity to respond to other pro-inflammatory stimuli, including LPS and pro-inflammatory cytokines (59, 60). Similarly, we observed heterogeneity in responses within astrocyte populations and across individual organoids. Some organoids and astrocyte subpopulations showed increased mitochondrial transcripts accumulating with interferon response genes as well as markers of reactivity and differentiation. Thus, this could be a mechanism for manganese-induced astrocyte reactivity found in postmortem brains of exposed individuals (13, 14).

The transcriptional signature in these reactive astrocytes shows a combination of deleterious markers such as reduced phagocytosis and high C3 expression, with neuron-supporting phenotypes, such as cholesterol biosynthesis, cytoskeleton genes involved in controlling cell area, and increased expression of glutamate transporters. Further studies are needed to clarify the role of these responses during manganese accumulation and toxicity in the brain.

We have identified type I interferon responses as a key pathway triggered during the first 24-48h following manganese exposure. Our findings are supported by published transcriptome datasets. These transcriptomes reveal manganese-dependent induction of interferon responses in human fetal astrocytes following a 7-day treatment in vitro (61). Bulk RNA transcriptomic studies in *Slc30a10*-deficient mice have shown upregulation of the astrocyte activation markers GFAP, CXCL10 and the interferon response genes Oas2 and 3 in brain, but not in liver (62). When specific brain sub regions of the basal ganglia in 1 month old *Slc30a10*-deficient mice were analyzed by bulk RNAseq, interferon responses were one of the major categories of genes upregulated in 2 of the 3 regions probed and was reversed when the manganese content in the diet was lowered (63). Since astrocytes have a high capacity for manganese uptake and have been shown to exhibit persistent activation in adult mice that were exposed as juveniles (64), the consequences of activation of interferon pathways elicited by a transient manganese exposure may extend even after removal of the toxic exposure. All cells in the brain express receptors for IFNβ, and a basal tone is required for normal development and cognition (65-67). Low levels of IFN production, specifically by astrocytes, has been shown to promote synaptic spine formation and cognitive function in hippocampus (68) and interferon responsive microglia have increased phagocytic activity towards neuronal bodies early in development (69). Complete absence of this pathway or excess is pathogenic. For example, interferon β or IFNR loss of function is sufficient to cause Parkinson's- like neurodegeneration (70) while excessive interferon beta contributes to

Alzheimer's disease in preclinical models and it is sufficient to cause synapse loss (71). Excess Interferon signaling is associated with Dystonia in Aicardi Goutieres syndrome (72) and secondary to Type I IFN therapy, which also induces psychiatric symptoms (66, 73). Cytokines produced by astrocytes exposed to manganese could be involved in mediating some of the cognitive outcomes associated with manganese exposures during early development, as well as cognitive and behavioral symptoms during early stages of disease in adults.

Mitochondrial DNA has been reported as a trigger of inflammation in several neurodegenerative diseases (74). Less is currently known about RNA from this organelle, but increased mitochondrial RNA has been found in the cytoplasm of neurons in mouse models of Huntington disease (75) and has been shown to drive inflammation in senescence (76). We postulate that mitochondrial dsRNA-dependent signaling could be a more general mechanism for triggering adaptive and maladaptive inflammation in diverse neurodegenerative disorders accounting for regionality within the brain or in between organs in manganese exposures or other genetic and environmental insults. Disruption of CRISPR screens suggest that RNA transcript processing and dsRNA formation in mitochondria are controlled by the function of multiple proteins in mitochondria and thereby could be influenced by signaling in the cytoplasm (36, 77). Hypoxia downregulates mitochondrial DNA transcription and the interferon pathway signaling in cancer cell lines (41, 78, 79). Metabolites generated by the mitochondrial enzymes fumarate hydratase (80) and aconitate decarboxylase (itaconate) (81) promote dsRNA accumulation and inflammatory responses. Altogether, these findings suggest that the mitochondrial transcriptome is affected and is an effector in manganese-induced cell signaling.

Methods:

Cell lines and media:
HAP1 wild type and SLC30A10$^{-/-}$ cells were grown in Iscove's DMEM 10%FBS at 37ºC and 5%CO_2. HeLa cells were grown in DMEM 10%FBS 10mM Glutamine at 37ºC and 5%CO_2. Human iPSCs were obtained through Emory Stem Cell and Organoids Core. This iPSC line was developed by reprogramming CD34+ human umbilical cord blood cells using an episomal system to deliver seven-factors: [SOKMNLT: SOX2, OCT4 (POU5F1), Kruppel-like factor 4 (KLF4), MYC (homologous to avian virus, myelocytomatosis oncogene), NANOG (homeobox transcription factor), LIN28 (regulates transition from pluripotency and committed cell lineages), and simian vacuolating virus 40 large (SV40L) T antigen] Epstein Barr nuclear antigen (EBNA). iPSCs were cultured in feeder-free conditions in dishes coated with Embryonic Stem Cell qualified Matrigel (Corning). iPSCs were negative for mycoplasma, passaged using ReLeSR (Stem Cell Technologies), cultured in StemFLex media (Thermo Fisher Scientific) and incubated at 37ºC and 5% CO_2. Astrocytes were differentiated and matured from neuroprogenitor cells employing StemCell differentiation and maturation media.
Cerebral organoids were developed as previously described (46, 47). On the first day, iPSCs were dissociated using Accutase (Stem Cell Technologies) and 18,000 cells were seeded for each organoid on 5-10 fiber scaffolds in low attachment plates. After 5 days, embryoid bodies were formed and transferred to induction media (Stem Cell Technologies) to direct them towards neuronal fate. After another 2 days, cells were expanded in Matrigel droplets for 3 days, then moved to organoid maturation media (Stem Cell Technologies). After 2 weeks in culture, the Matrigel was removed from the organoids by mechanical dissociation and the organoids were grown on an orbital shaker (Infors HT). Maturation media was changed twice a week during organoids growth for up to 100 days in culture.

Transfections and luciferase measurements:
Stable cell lines were generated by transfection of HAP1 and HeLa cells with Lipofectamine 3000 (Invitrogen) and plasmid pNiFty3-L-Fluc-Puro (InvivoGen) followed by selection in media containing 5μg/ml Puromycin (Gibco). High Molecular weight Poly I:C (InvivoGen) was delivered at 1μg/ml by direct addition to the media at the time of Manganese treatment. The Sting agonist 2'3' cdAM(PS)2 (ADU-S100) was delivered by transfection with Lipofectamine 3000. Following 24h treatment, the cells were washed with PBS, incubated with luciferase substrate Bright Glo (Promega) for 10minutes at room temperature before luminescence measured in a white plate. SiRNA (Dharmacon) was delivered at 50nM by two sequential reverse transfections (at day 1 and 3) with RNA-Max (Invitrogen). Cells were treated at day 5 post-transfection and analyzed at day 6. Percentage of inhibition was calculated using as a reference the fold of change induced by manganese treatment in scrambled siRNA transfected cells.

Immunoblot:
At the moment of analysis, cells grown in 6 well plates were washed with cold phosphate-buffered saline (PBS) and lysed in buffer containing 10 mM HEPES pH 7.4, 150 mM NaCl, 1 mM ethylene glycol-bis(β-aminoethylether)-*N*,*N*,*N*′,*N*′-tetraacetic acid (EGTA), and 0.1 mM MgCl2, (Buffer A), with 0.5% Triton X-100 and Complete anti-protease. Cells were then scraped and placed in 1.5ml tubes on ice for 20 min and centrifuged at 21130rcf for 15 min. Protein was measured in the clarified supernatant with Bradford Assay. Proteins were reduced and denatured with Laemmli buffer and heated for 5 min at 75ºC and separated by SDS-PAGE in 4-20% Criterion gels and transferred using the semidry transfer method to polyvinylidene difluoride (PVDF) membranes. The membranes were blocked in TBS containing 5% nonfat milk and 0.05% Triton X-100 for 1h at room temperature and incubated overnight with primary antibody prepared in PBS with 3% bovine serum albumin (BSA) and 0.2% sodium azide at 4ºC.

Detection HRP labelled secondary were diluted 1:5000 and enzymatic activity was detected with Western Lightning Plus ECL substrate (PerkinElmer, NEL105001EA) and exposure to GE Healthcare Hyperfilm ECL (28906839).

Immunofluorescence:
Cells were fixed in 4% PFA at 37ºC for 20 minutes and permeabilized with 0.25% triton X100 on ice for 5 minutes. For dsRNA detection, permeabilization included 20U/ml SUPERase-In RNAse inhibitor. Control wells were treated with 5U/ml RNAseIII in PBS with 10mM $MgCl_2$ for 30 min at 37ºC in PBS. After blocking, J2 antibody 1:300, GRSF1 1:500, Tom20 1:300, GFAP 1:300 were used. Slides were imaged in a Nikon A1R HD25 confocal microscope with a 60x Apo lens (NA=1.4,WD=140uM).DsRNA localized to the mitochondrial granule positive for GSRF1 was quantified with Image J/Fiji software in the focal plane of maximal intensity of a Z-stack. On both images, background was subtracted with a 30 radius and signal was thresholded. Measurements of fluorescence of dsRNA per cell were directed and limited to the corresponding GSRF1 image. At least 30 cells in a minimum of 5 fields were measured. Organoids were fixed overnight in 4%PFA and then incubated in sucrose before embedding. 8μm paraffin sections were re-hydrated by alcohol dilution series washes and antigen retrieval was performed for 20min in Citrate buffer pH6 with 0.05% Tween at 60% power in the microwave and then stained as described above. Organoid images were corrected by brightness and contrast to distinguish positive from negative cells and background signal. Cells within 300μm from the organoid surface, in 5 different captured fields were identified as GFAP positive and then classified as dsRNA positive or negative. Identical scoring was obtained by two independent observers.

Cytokine measurements:
Human Cytokine Array (R&D Systems) were used to profile cytokines in conditioned media following 48h manganese treatment in HeLa (750μM) and Hap1(150μM) cells. A high and a low exposure film was quantified by thresholding and measuring the signal intensity with the circular brush selection in FIJI/Image J on each spot and an equal adjacent area to subtract local background. CXCL8/IL8 was measured in media conditioned for 48h employing Elisa assays (BioLegend and R&D) following manufacturer's protocols. The human Proinflammatory 9-Plex panel from MesoScale and the R-PLEX Human B2M Antibody Set were employed to measure cytokines and beta 2 microglobulin in conditioned media from organoid treated for 48h by the Emory Multiplexed Immunoassay Core.

Cell survival assay:
Cells were counted using an automated Bio-Rad cell counter (Bio-Rad, TC20) and plated in 96 well plates at 2,000 cells/well and allowed to sit overnight before drugs were added. Cells were treated with the drug concentrations indicated in each figure for 72 hours when fresh media with 10% Alamar blue (Resazurin, R&D Systems) was added to each well and incubated for 2 hours at 37ºC.Fluorescence excitation at 530–570 nm and emission maximum at 580–590 nm was measured using a microplate reader using a BioTek Synergy HT microplate reader with Gen5 software 3.11. For each experiment, percent survival was calculated by subtracting the background value of an empty well with only Alamar blue and normalizing to the untreated condition for each genotype. Individual data points represent the average survival of duplicate or triplicate treatments for each concentration.

Total RNA extraction and NanoString mRNA Quantification
Cells were grown on 10 cm plates and after treatment, washed twice in ice-cold PBS and solubilized in 1 ml of TRIzol (Invitrogen). RNA Extraction and NanoString processing was completed by the Emory Integrated Genomics Core. RNA quality was assessed by bioanalyzer before proceeding with the NanoString probe hybridization. The NanoString Neuroinflammation

gene panel kit or a custom panel MitoString was used for mRNA quantification. mRNA counts were normalized the housekeeping genes TBP for the neuroinflammatory panel and CLCT for the MitoString using nSolver. Normalized data were further processed and visualized by Qlucore.

Cytokine /Chemokine Multiplex Luminex Immunoassay:
Frozen mouse brain samples were provided by Dr. Tom Bartnikas. Shavings of frozen tissue were collected and lysed in 8M urea in 100mM PO_4 with Complete anti-protease and PhosSTOP phosphatase inhibitor and homogenized by sonication (Fisher Scientific, Sonic Dismembrator Model 100). After incubation on ice for 30 minutes, samples were spun at 7000 × g for 10 minutes at 4C, and the supernatant was transferred to a new tube. Protein concentration was measured in triplicate using the Pierce BCA Protein Assay Kit (Thermo Fisher Scientific) according to manufacturer protocol. 5 µg of brain and 15 µg of liver tissue samples were diluted using urea buffer and analyzed using the Milliplex MAP Mouse Cytokine/Chemokine Multiplex assay (Millipore Sigma, St. Louis, MO, USA, MCYTMAG-70K-PX32) Eotaxin/CCL11, G-CSF, GM-CSF, IFN-γ, IL-1α, IL-1β, IL-2, IL-3, IL-4, IL-5, IL-6, IL-7, IL-9, IL-10, IL-12 (p40), IL-12 (p70), IL-13, IL-15, IL-17, IP-10, KC, LIF, LIX, MCP-1, M-CSF, MIG, MIP-1α, MIP-1β, MIP-2, RANTES, TNF-α, VEGF. Assays were read out with a MAGPIX Luminex instrument (Luminex, Austin, TX, USA).

ICP mass spectrometry:
Procedures were performed as described previously (82). Briefly, cells were plated on 10 cm dishes. After reaching desired confluency, cells were treated for 24 hours. At sample collection, the plates were washed three times with PBS, detached with trypsin, and neutralized with media and pelleted at 800 × g for 5 min at 4C. The cell pellet was resuspended with ice-cold PBS, aliquoted into 3-5 tubes, centrifuged at 2000rpm for 3 min Cell pellets were stored at -80C. The pellets were digested by adding 50 µL of 70% trace metal basis grade nitric acid followed by heating at 95ºC for 10 min. After cooling, 20 µL of each sample was diluted to 800 µL to a final concentration of 2% nitric acid using either 2% nitric acid or 2% nitric acid with 0.5% hydrochloric acid (vol/vol). Metal levels were quantified using a triple quad ICP-MS instrument (Thermo Fisher, iCAP-TQ) operating in oxygen mode under standard conditions (RF power 1550 W, sample depth 5.0 mm, nebulizer flow 1.12L/min, spray chamber 3C, extraction lens 1,2 -195, —15 V). Oxygen was used as a reaction gas (0.3 mL/min) to remove polyatomic interferences or mass shift target elements. External calibration curves were generated using a multielemental standard (ICP-MSCAL2-1, AccuStandard, USA) and ranged from 0.5 to 1000 µg/L for each element. Scandium (10 µg/L) was used as internal standard and diluted into the sample in-line. Samples were introduced into the ICP-MS using the 2DX PrepFAST M5 autosampler (Elemental Scientific) equipped with a 250 µL loop and using the 0.25 mL precision method provided by the manufacturer. Serumnorm (Sero, Norway) was used as a standard reference material, and values for elements of interest were within 20% of the accepted value. Quantitative data analysis was conducted with Qtegra software, and values were exported to Excel for further statistical analysis.
Cell isolation and capture for single cell RNAseq:
Organoids were dissociated into a single cell suspension using previously published methods (83) adapted for organoids dissociation by decreasing volumes and omission of filtering steps. Briefly, organoid tissue was chopped using a scalpel and digested in 10ml with 25 U/ml papain (Worthington) and 12.5 U/ml DNAseI (Worthington) in a 5% CO2 incubator at 34ºC on an orbital shaker at 123rpm for 45 min. Cells were washed with a protease inhibitor solution (ovomucoid). Following addition of Ovomucoid, the tissue was further triturated by pipetting and once single cell suspensions achieved, the cells were collected by centrifugation. All dissociation and trituration steps were performed in the presence of Protector RNAse inhibitor (Sigma

03335402001), transcription inhibitor actinomycin D (Sigma-Aldrich; Cat#: A1410), and translation inhibitor anisomycin (Sigma-Aldrich; Cat#: A9789) based on published recommendations (84). Up to 10,000 cells per organoid were captured with a Chromium GEM-X-Single Cell 3' Chip kit v4 from 10X Genomics. Libraries were prepared using Chromium Next GEM Single Cell 3' Kit v4 (1000686) with dual index labeling and sequenced on a standard Illumina platform.

Statistical analyses

NanoString data was normalized with nCounter and then processed with Qlucore Omics Explorer Version 3.6(33). ANOVA and paired analyses were conducted with Prism Version 10.2.2 (341). Gene ontology studies were performed with ENRICHR (85).

Luminex Cytokine Statistical and Multivariate Analyses, Wilcoxon rank sum test was performed in R. Partial least squares regressions (PLSRs) and discriminant PLSRs (D-PLSRs) were performed in R using the *ropls* package v1.4.2. The data were z-scored before being input into the function. Cytokine measurements were used as the independent variables, and the discrete regression variable in all D-PLSR analyses was genotype/sex. Error bars for LV loadings were calculated by iteratively excluding K samples without replacement 100 times (leave-K-out cross-validation, LKOCV), and regenerating the D-PLSR model each time. Error bars in the LV1 plots report the mean and SD computed across the models generated to provide an indication of the variability within each cytokine among the models generated.

Single-cell sequencing analysis

The sequencing data were aligned to the human genome and demultiplexed using Cellranger. Analysis was performed in R Studio using Seurat. For quality control, cells with <8% mitochondrial genes were excluded and ncounts were filtered for 500-8000 range. Cells were integrated and normalized using SCT transform to generate a UMAP and clustering based on based on shared nearest neighbors. All featureplots, dot plots, and differential expression are based on non-transformed RNA counts. Differential expression was performed using pseudobulk data aggregation and Findmarkers DeSEQ2. Heatmaps are based in scaled RNA counts data.

References:

1. R. C. Balachandran *et al.*, Brain manganese and the balance between essential roles and neurotoxicity. *J Biol Chem* **295**, 6312-6329 (2020).
2. T. V. Peres *et al.*, "Manganese-induced neurotoxicity: a review of its behavioral consequences and neuroprotective strategies". *BMC Pharmacol Toxicol* **17**, 57 (2016).
3. E. L. Lucas *et al.*, Impact of ferromanganese alloy plants on household dust manganese levels: implications for childhood exposure. *Environ Res* **138**, 279-290 (2015).
4. E. S. Kornblith, S. L. Casey, D. T. Lobdell, M. A. Colledge, R. M. Bowler, Environmental exposure to manganese in air: Tremor, motor and cognitive symptom profiles. *Neurotoxicology* **64**, 152-158 (2018).
5. J. Schullehner *et al.*, Exposure to Manganese in Drinking Water during Childhood and Association with Attention-Deficit Hyperactivity Disorder: A Nationwide Cohort Study. *Environ Health Perspect* **128**, 97004 (2020).
6. C. J. Mercadante *et al.*, Manganese transporter Slc30a10 controls physiological manganese excretion and toxicity. *J Clin Invest* **129**, 5442-5461 (2019).
7. A. N. Rodichkin, T. R. Guilarte, Hereditary Disorders of Manganese Metabolism: Pathophysiology of Childhood-Onset Dystonia-Parkinsonism in SLC39A14 Mutation Carriers and Genetic Animal Models. *Int J Mol Sci* **23** (2022).
8. C. A. Taylor *et al.*, SLC30A10 transporter in the digestive system regulates brain manganese under basal conditions while brain SLC30A10 protects against neurotoxicity. *J Biol Chem* **294**, 1860-1876 (2019).
9. R. Lucchini *et al.*, Long-term exposure to "low levels" of manganese oxides and neurofunctional changes in ferroalloy workers. *Neurotoxicology* **20**, 287-297 (1999).
10. S. Anagianni, K. Tuschl, Genetic Disorders of Manganese Metabolism. *Curr Neurol Neurosci Rep* **19**, 33 (2019).
11. D. Mergler *et al.*, Manganese neurotoxicity, a continuum of dysfunction: results from a community based study. *Neurotoxicology* **20**, 327-342 (1999).
12. C. W. Olanow, Manganese-induced parkinsonism and Parkinson's disease. *Ann N Y Acad Sci* **1012**, 209-223 (2004).
13. D. P. Perl, C. W. Olanow, The neuropathology of manganese-induced Parkinsonism. *J Neuropathol Exp Neurol* **66**, 675-682 (2007).
14. L. F. Gonzalez-Cuyar *et al.*, Quantitative neuropathology associated with chronic manganese exposure in South African mine workers. *Neurotoxicology* **45**, 260-266 (2014).
15. T. Vezer, A. Kurunczi, M. Naray, A. Papp, L. Nagymajtenyi, Behavioral effects of subchronic inorganic manganese exposure in rats. *Am J Ind Med* **50**, 841-852 (2007).
16. J. M. Antonini *et al.*, Mild steel welding fume causes manganese accumulation and subtle neuroinflammatory changes but not overt neuronal damage in discrete brain regions of rats after short-term inhalation exposure. *Neurotoxicology* **30**, 915-925 (2009).
17. N. M. Filipov, C. A. Dodd, Role of glial cells in manganese neurotoxicity. *J Appl Toxicol* **32**, 310-317 (2012).
18. R. B. Tjalkens, K. A. Popichak, K. A. Kirkley, Inflammatory Activation of Microglia and Astrocytes in Manganese Neurotoxicity. *Adv Neurobiol* **18**, 159-181 (2017).
19. X. M. Fan *et al.*, Chronic Manganese Administration with Longer Intervals Between Injections Produced Neurotoxicity and Hepatotoxicity in Rats. *Neurochem Res* **45**, 1941-1952 (2020).
20. J. Soto-Verdugo, A. Ortega, Critical Involvement of Glial Cells in Manganese Neurotoxicity. *Biomed Res Int* **2021**, 1596185 (2021).
21. M. Sidoryk-Wegrzynowicz, M. Aschner, Role of astrocytes in manganese mediated neurotoxicity. *BMC Pharmacol Toxicol* **14**, 23 (2013).

22. K. S. Kirkley, K. A. Popichak, M. F. Afzali, M. E. Legare, R. B. Tjalkens, Microglia amplify inflammatory activation of astrocytes in manganese neurotoxicity. *J Neuroinflammation* **14**, 99 (2017).
23. P. Zhang *et al.*, Microglia enhance manganese chloride-induced dopaminergic neurodegeneration: role of free radical generation. *Exp Neurol* **217**, 219-230 (2009).
24. K. A. Popichak, M. F. Afzali, K. S. Kirkley, R. B. Tjalkens, Glial-neuronal signaling mechanisms underlying the neuroinflammatory effects of manganese. *J Neuroinflammation* **15**, 324 (2018).
25. T. C. Frank-Cannon, L. T. Alto, F. E. McAlpine, M. G. Tansey, Does neuroinflammation fan the flame in neurodegenerative diseases? *Mol Neurodegener* **4**, 47 (2009).
26. C. K. Glass, K. Saijo, B. Winner, M. C. Marchetto, F. H. Gage, Mechanisms underlying inflammation in neurodegeneration. *Cell* **140**, 918-934 (2010).
27. E. Werner *et al.*, The mitochondrial RNA granule modulates manganese-dependent cell toxicity. *Mol Biol Cell* **33**, ar108 (2022).
28. A. R. D'Souza, M. Minczuk, Mitochondrial transcription and translation: overview. *Essays Biochem* **62**, 309-320 (2018).
29. W. I. Murphy, B. Attardi, C. Tu, G. Attardi, Evidence for complete symmetrical transcription in vivo of mitochondrial DNA in HeLa cells. *J Mol Biol* **99**, 809-814 (1975).
30. G. Santonoceto, A. Jurkiewicz, R. J. Szczesny, RNA degradation in human mitochondria: the journey is not finished. *Hum Mol Genet* **33**, R26-R33 (2024).
31. G. Barshad, S. Marom, T. Cohen, D. Mishmar, Mitochondrial DNA Transcription and Its Regulation: An Evolutionary Perspective. *Trends Genet* **34**, 682-692 (2018).
32. Y. G. Chen, S. Hur, Cellular origins of dsRNA, their recognition and consequences. *Nat Rev Mol Cell Biol* **23**, 286-301 (2022).
33. J. Grochowska, J. Czerwinska, L. S. Borowski, R. J. Szczesny, Mitochondrial RNA, a new trigger of the innate immune system. *Wiley Interdiscip Rev RNA* **13**, e1690 (2022).
34. M. Quadri *et al.*, Mutations in SLC30A10 cause parkinsonism and dystonia with hypermanganesemia, polycythemia, and chronic liver disease. *Am J Hum Genet* **90**, 467-477 (2012).
35. K. Tuschl *et al.*, Syndrome of hepatic cirrhosis, dystonia, polycythemia, and hypermanganesemia caused by mutations in SLC30A10, a manganese transporter in man. *Am J Hum Genet* **90**, 457-466 (2012).
36. A. R. Wolf, V. K. Mootha, Functional genomic analysis of human mitochondrial RNA processing. *Cell Rep* **7**, 918-931 (2014).
37. J. Schonborn *et al.*, Monoclonal antibodies to double-stranded RNA as probes of RNA structure in crude nucleic acid extracts. *Nucleic Acids Res* **19**, 2993-3000 (1991).
38. N. A. Bonekamp *et al.*, Small-molecule inhibitors of human mitochondrial DNA transcription. *Nature* **588**, 712-716 (2020).
39. C. P. Chan, D. Y. Jin, Cytoplasmic RNA sensors and their interplay with RNA-binding partners in innate antiviral response: theme and variations. *RNA* **28**, 449-477 (2022).
40. A. Dhir *et al.*, Mitochondrial double-stranded RNA triggers antiviral signalling in humans. *Nature* **560**, 238-242 (2018).
41. E. Arnaiz *et al.*, Hypoxia Regulates Endogenous Double-Stranded RNA Production via Reduced Mitochondrial DNA Transcription. *Front Oncol* **11**, 779739 (2021).
42. M. Luna-Sanchez, P. Bianchi, A. Quintana, Mitochondria-Induced Immune Response as a Trigger for Neurodegeneration: A Pathogen from Within. *Int J Mol Sci* **22** (2021).
43. A. Carrer, C. Laquatra, L. Tommasin, M. Carraro, Modulation and Pharmacology of the Mitochondrial Permeability Transition: A Journey from F-ATP Synthase to ANT. *Molecules* **26** (2021).
44. J. P. Choi *et al.*, Cytokine Inductions and Intracellular Signal Profiles by Stimulation of dsRNA and SEB in the Macrophages and Epithelial Cells. *Immune Netw* **22**, e15 (2022).

45. A. Shkundin, A. Halaris, IL-8 (CXCL8) Correlations with Psychoneuroimmunological Processes and Neuropsychiatric Conditions. *J Pers Med* **14** (2024).
46. M. A. Lancaster *et al.*, Cerebral organoids model human brain development and microcephaly. *Nature* **501**, 373-379 (2013).
47. M. A. Lancaster *et al.*, Guided self-organization and cortical plate formation in human brain organoids. *Nat Biotechnol* **35**, 659-666 (2017).
48. K. M. Erikson, A. W. Dobson, D. C. Dorman, M. Aschner, Manganese exposure and induced oxidative stress in the rat brain. *Sci Total Environ* **334-335**, 409-416 (2004).
49. A. Liberzon *et al.*, The Molecular Signatures Database (MSigDB) hallmark gene set collection. *Cell Syst* **1**, 417-425 (2015).
50. J. Holzmann *et al.*, RNase P without RNA: identification and functional reconstitution of the human mitochondrial tRNA processing enzyme. *Cell* **135**, 462-474 (2008).
51. M. Szewczyk *et al.*, Human REXO2 controls short mitochondrial RNAs generated by mtRNA processing and decay machinery to prevent accumulation of double-stranded RNA. *Nucleic Acids Res* **48**, 5572-5590 (2020).
52. L. B. Wood *et al.*, Identification of neurotoxic cytokines by profiling Alzheimer's disease tissues and neuron culture viability screening. *Sci Rep* **5**, 16622 (2015).
53. P. Geladi, B. R. Kowalski, An example of 2-block predictive partial least-squares regression with simulated data. *Analytica Chimica Acta* **185**, 19-32 (1986).
54. I. Barroeta-Espar *et al.*, Distinct cytokine profiles in human brains resilient to Alzheimer's pathology. *Neurobiol Dis* **121**, 327-337 (2019).
55. M. Prajapati *et al.*, Hepatic HIF2 is a key determinant of manganese excess and polycythemia in SLC30A10 deficiency. *JCI Insight* **9** (2024).
56. Y. Kim *et al.*, PKR Senses Nuclear and Mitochondrial Signals by Interacting with Endogenous Double-Stranded RNAs. *Mol Cell* **71**, 1051-1063 e1056 (2018).
57. H. Sui, Q. Chen, J. Yang, S. Srirattanapirom, T. Imamichi, Manganese enhances DNA- or RNA-mediated innate immune response by inducing phosphorylation of TANK-binding kinase 1. *iScience* **25**, 105352 (2022).
58. D. W. Chan *et al.*, Purification and characterization of ATM from human placenta. A manganese-dependent, wortmannin-sensitive serine/threonine protein kinase. *J Biol Chem* **275**, 7803-7810 (2000).
59. P. Hasel, I. V. L. Rose, J. S. Sadick, R. D. Kim, S. A. Liddelow, Neuroinflammatory astrocyte subtypes in the mouse brain. *Nat Neurosci* **24**, 1475-1487 (2021).
60. F. Endo *et al.*, Molecular basis of astrocyte diversity and morphology across the CNS in health and disease. *Science* **378**, eadc9020 (2022).
61. A. Sengupta *et al.*, Gene expression profiling of human primary astrocytes exposed to manganese chloride indicates selective effects on several functions of the cells. *Neurotoxicology* **28**, 478-489 (2007).
62. M. Prajapati *et al.*, AAV-mediated hepatic expression of SLC30A10 and the Thr95Ile variant attenuates manganese excess and other phenotypes in Slc30a10-deficient mice. *J Biol Chem* **300**, 105732 (2024).
63. A. Warden *et al.*, Loss of SLC30A10 manganese transporter alters expression of neurotransmission genes and activates hypoxia-inducible factor signaling in mice. *Metallomics* **16** (2024).
64. J. A. Moreno *et al.*, Age-dependent susceptibility to manganese-induced neurological dysfunction. *Toxicol Sci* **112**, 394-404 (2009).
65. T. Blank, M. Prinz, Type I interferon pathway in CNS homeostasis and neurological disorders. *Glia* **65**, 1397-1406 (2017).
66. B. Viengkhou, M. J. Hofer, Breaking down the cellular responses to type I interferon neurotoxicity in the brain. *Front Immunol* **14**, 1110593 (2023).

67. T. J. Dorrity, H. Shin, J. A. Gertie, H. Chung, The Sixth Sense: Self-nucleic acid sensing in the brain. *Adv Immunol* **161**, 53-83 (2024).
68. S. Hosseini *et al.*, Type I Interferon Receptor Signaling in Astrocytes Regulates Hippocampal Synaptic Plasticity and Cognitive Function of the Healthy CNS. *Cell Rep* **31**, 107666 (2020).
69. C. C. Escoubas *et al.*, Type-I-interferon-responsive microglia shape cortical development and behavior. *Cell* **187**, 1936-1954 e1924 (2024).
70. P. Ejlerskov *et al.*, Lack of Neuronal IFN-beta-IFNAR Causes Lewy Body- and Parkinson's Disease-like Dementia. *Cell* **163**, 324-339 (2015).
71. E. R. Roy *et al.*, Type I interferon response drives neuroinflammation and synapse loss in Alzheimer disease. *J Clin Invest* **130**, 1912-1930 (2020).
72. I. Peixoto de Barcelos *et al.*, Systemic complications of Aicardi Goutieres syndrome using real-world data. *Mol Genet Metab* **143**, 108578 (2024).
73. P. Zhang *et al.*, Dystonia during pegylated interferon alpha therapy in a case with essential thrombocythemia and cerebral infarction. *Neurol Sci* **45**, 5943-5945 (2024).
74. B. D. Paul, S. H. Snyder, V. A. Bohr, Signaling by cGAS-STING in Neurodegeneration, Neuroinflammation, and Aging. *Trends Neurosci* **44**, 83-96 (2021).
75. H. Lee *et al.*, Cell Type-Specific Transcriptomics Reveals that Mutant Huntingtin Leads to Mitochondrial RNA Release and Neuronal Innate Immune Activation. *Neuron* **107**, 891-908 e898 (2020).
76. V. Lopez-Polo *et al.*, Release of mitochondrial dsRNA into the cytosol is a key driver of the inflammatory phenotype of senescent cells. *Nat Commun* **15**, 7378 (2024).
77. S. Kim *et al.*, RNA 5-methylcytosine marks mitochondrial double-stranded RNAs for degradation and cytosolic release. *Mol Cell* **84**, 2935-2948 e2937 (2024).
78. T. Peng, S. Y. Du, M. Son, B. Diamond, HIF-1alpha is a negative regulator of interferon regulatory factors: Implications for interferon production by hypoxic monocytes. *Proc Natl Acad Sci U S A* **118** (2021).
79. A. Miar *et al.*, Hypoxia Induces Transcriptional and Translational Downregulation of the Type I IFN Pathway in Multiple Cancer Cell Types. *Cancer Res* **80**, 5245-5256 (2020).
80. A. Hooftman *et al.*, Macrophage fumarate hydratase restrains mtRNA-mediated interferon production. *Nature* **615**, 490-498 (2023).
81. S. M. O'Carroll *et al.*, Itaconate drives mtRNA-mediated type I interferon production through inhibition of succinate dehydrogenase. *Nat Metab* **6**, 2060-2069 (2024).
82. A. Lane *et al.*, Sulfur- and phosphorus-standardized metal quantification of biological specimens using inductively coupled plasma mass spectrometry. *STAR Protoc* **3**, 101334 (2022).
83. Y. Zhang *et al.*, Purification and Characterization of Progenitor and Mature Human Astrocytes Reveals Transcriptional and Functional Differences with Mouse. *Neuron* **89**, 37-53 (2016).
84. S. E. Marsh *et al.*, Dissection of artifactual and confounding glial signatures by single-cell sequencing of mouse and human brain. *Nat Neurosci* **25**, 306-316 (2022).
85. Z. Xie *et al.*, Gene Set Knowledge Discovery with Enrichr. *Curr Protoc* **1**, e90 (2021).

Figures with Legends:

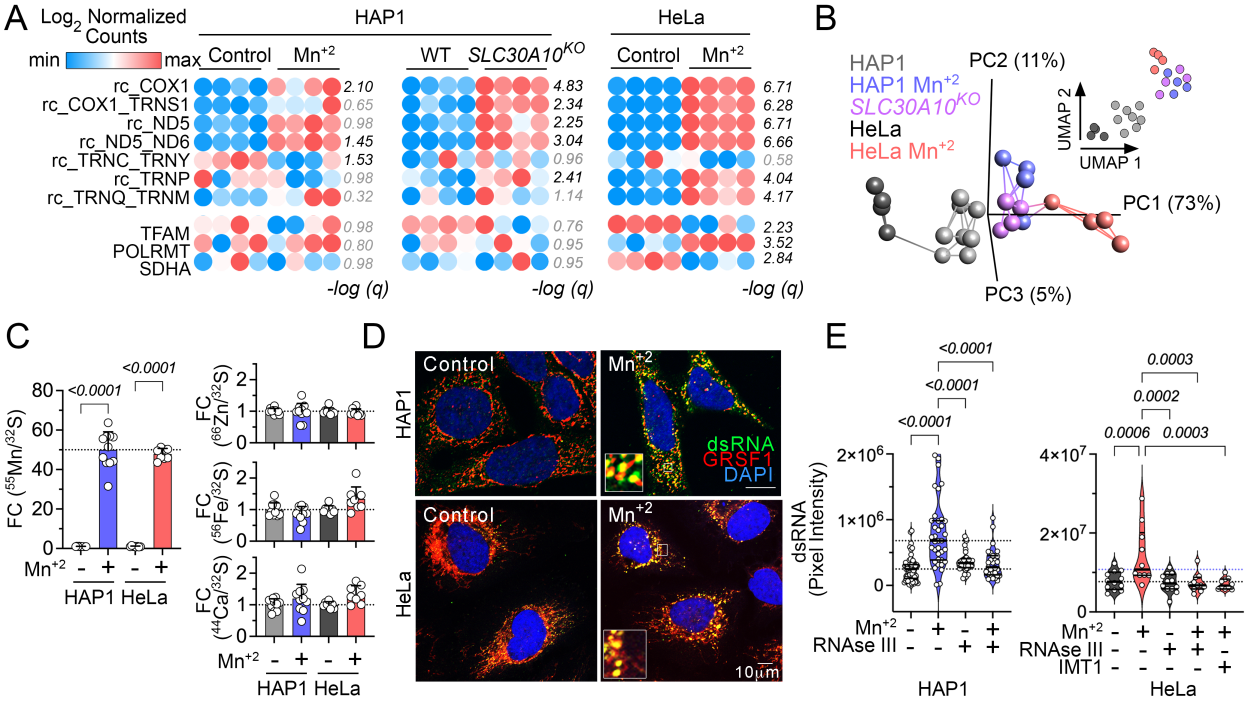

Figure 1: Manganese induces the accumulation of noncoding mitochondrial RNA sequences and mitochondrial dsRNA

a) Heatmaps of log_2 CLTC normalized NanoString counts of RNA hybridized with probes targeted to non-coding sequences of the light strand of mitochondrial transcripts and for nuclear encoded mitochondrial proteins as control. RNA was isolated from four replicate samples of either wild-type HAP1 or HeLa treated either in the absence or presence of manganese (300µM and 800µM, respectively) for 24h, or untreated wild-type and SLC30A10 null HAP1 cells. Numbers in italics represent -log10 p values (t-test followed by Benjamini-Hochberg FDR correction, *q*).

b) Manganese treatment and SLC30A10 deficiency similarly alter the MitoString transcriptome. Linear and non-linear data reduction by principal component analysis (PCA) and Uniform Manifold Approximation and Projection (UMAP), respectively of all the RNA counts measured by the MitoString panel. Lines connecting PCA represent Euclidean distances.

c) Metal content of HAP1 or HeLa cells treated in the absence or presence of manganese as in (a). Manganese, zinc, iron and calcium levels are depicted as sulphur-normalized metal content measured by ICP-MS at 24h. Fold of change (FC) after manganese

addition. Data from two experiments are combined. One-way ANOVA followed by Šídák's multiple comparisons test.

d) Immunofluorescence detection of dsRNA and the mitochondrial RNA granule component, GSRF1, in HAP1 and HeLa cells treated either in the absence or presence of manganese.

e) Quantification of dsRNA overlapping with GRSF1 in cells treated either in the absence or presence manganese, the POLMRT inhibitor IMT1 (1μM), or with dsRNA specific RNAse III before addition of the dsRNA J2 antibody. Dotted lines represent the average intensity of cells treated in the absence or presence manganese. One-way ANOVA followed by Šídák's multiple comparisons tests.

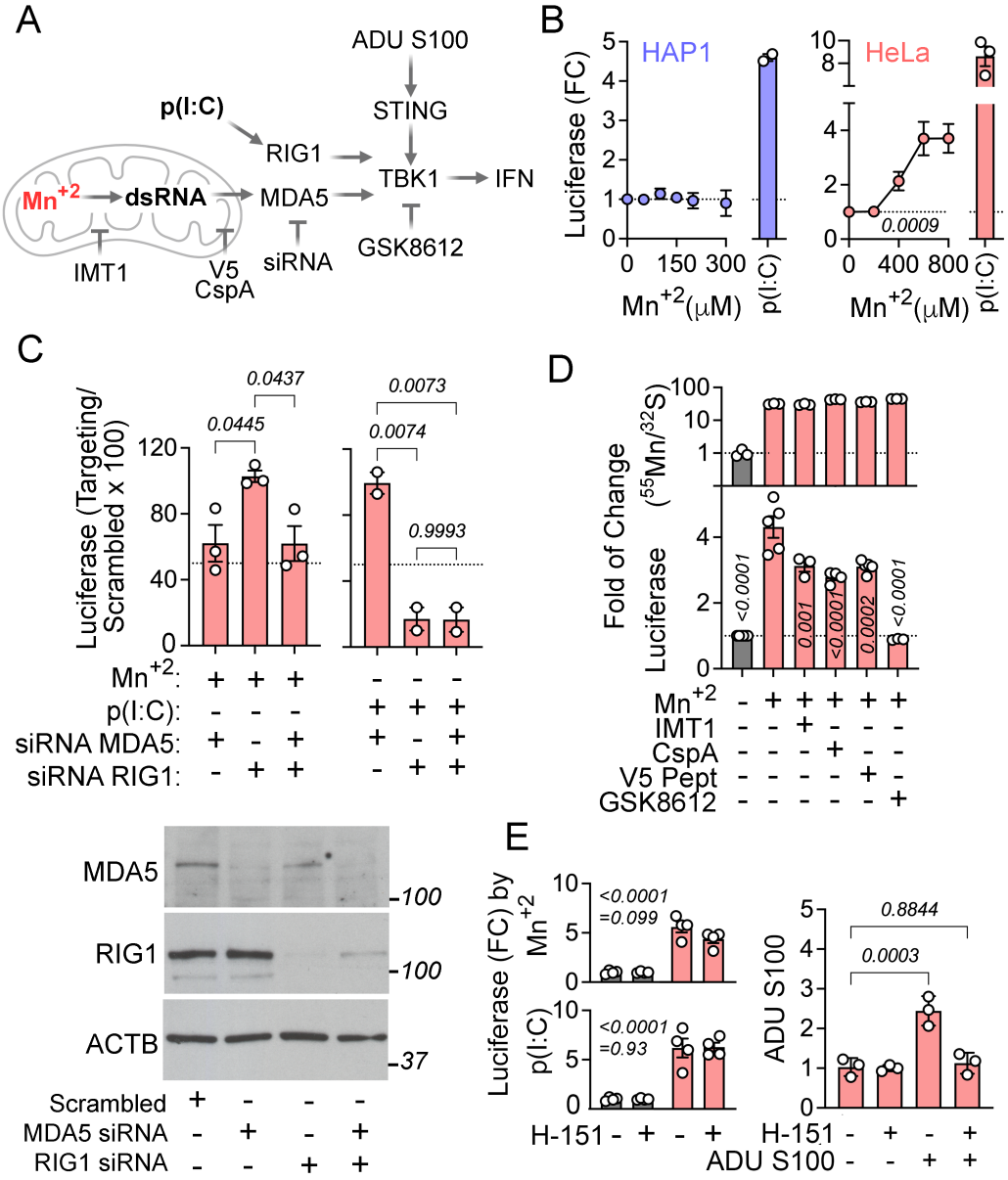

Figure 2: Manganese-induced dsRNA upregulates interferon β transcription.

a) Diagram summarizing the pathway activated by manganese effects in mitochondria leading to IFNβ transcription. Depicted are the components targeted by inhibitors and the pathway agonists, poly (I:C) and ADU S100.

b) Interferon β promoter luciferase reporter activity measured in either HAP1 or HeLa cells following 24h treatment with the indicated manganese dose. For positive control 10μg/ml of high molecular weight poly (I:C) were added. Average ± SEM of 3 experiments. One-

way ANOVA followed by Dunnett's multiple comparisons test. Dotted line marks luciferase activity in the absence of manganese.

c) Interferon β promoter luciferase reporter activity measured in HeLa cells transfected with non-targeting and targeting siRNAs followed by 24h treatment with 800μM manganese or 10 μg/ml poly (I:C). Data are depicted as percentage of signal in scrambled sequence siRNA transfected cells. Average ± SEM of 3 experiments. Dotted line marks 50% reduction. One-way ANOVA followed by Tukey's multiple comparisons test. Bottom panel depicts western blots of protein level downregulation following siRNA transfections.

d) Top panel depicts manganese content determined by ICP-MS in HeLa cells incubated with 800μM manganese with and without the indicated inhibitor, identical conditions as employed for the bottom panel experiments. Bottom panel shows luciferase activity measured in HeLa cells following 24h treatment with the indicated manganese dose. For positive control, 10μg/ml of poly (I:C) were added. Average ± SEM of 5 experiments. Two-way ANOVA followed by Bonferroni's multiple comparisons test.

e) Luciferase activity measured in HeLa cells following 24h treatment with 800μM manganese (top left panel) or 10μg/ml poly(I:C) (bottom left panel) in the presence or absence of the Sting inhibitor H-151. Right panel shows 0.5μM H-151 inhibition of luciferase induction by transfection of 1μM ADU S100 Sting agonist. Average± SE. Two-way ANOVA followed by Bonferroni's multiple comparisons test. Top numbers show manganese effect, bottom number show drug effect.

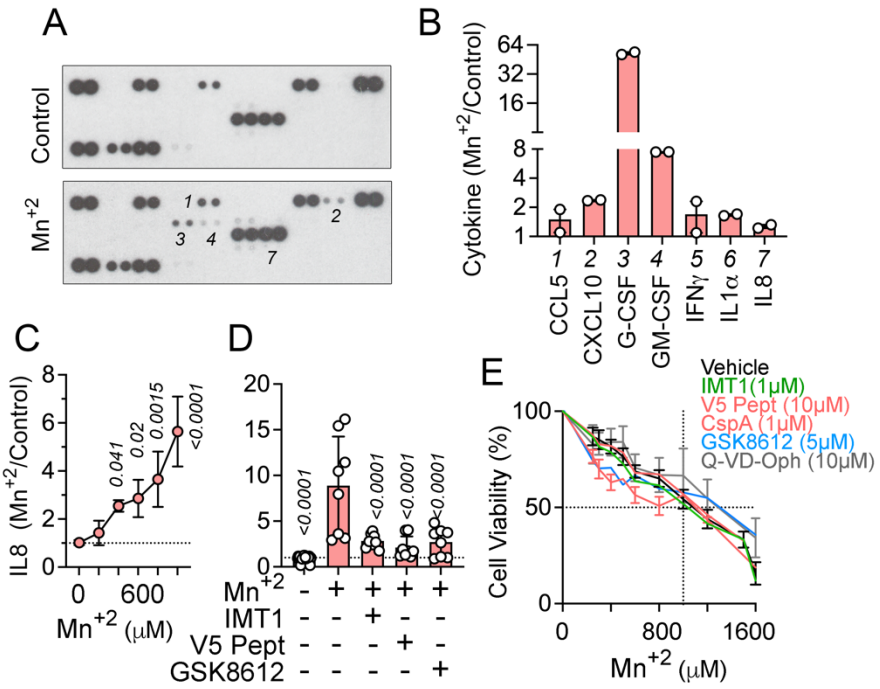

Figure 3: Manganese upregulates inflammatory cytokine secretion.

a) Inflammatory cytokine antibody array probed with media conditioned for 48h collected from treated HeLa cells without or with 750μM manganese.

b) Densitometry quantification of positive spots in the array blots shown in (a) and Fig S1A.

c) IL-8 cytokine levels measured by ELISA in 48h conditioned media collected from HeLa cells treated without or with the indicated manganese concentration. Average ± SEM of 3 experiments. One-way ANOVA followed by Dunnett's multiple comparisons test.

d) IL-8 cytokine levels measured by ELISA in 48h conditioned media collected from HeLa cells treated without or with 800μM manganese and the indicated inhibitor. Average ± SEM of 4 experiments. One-way ANOVA followed by Dunnett's multiple comparisons test

e) Cell survival of HeLa cells exposed to increased concentrations of manganese with and without the indicated inhibitor. Average ± SEM of 3-4 experiments. Two-way ANOVA followed by Bonferroni's multiple comparisons test.

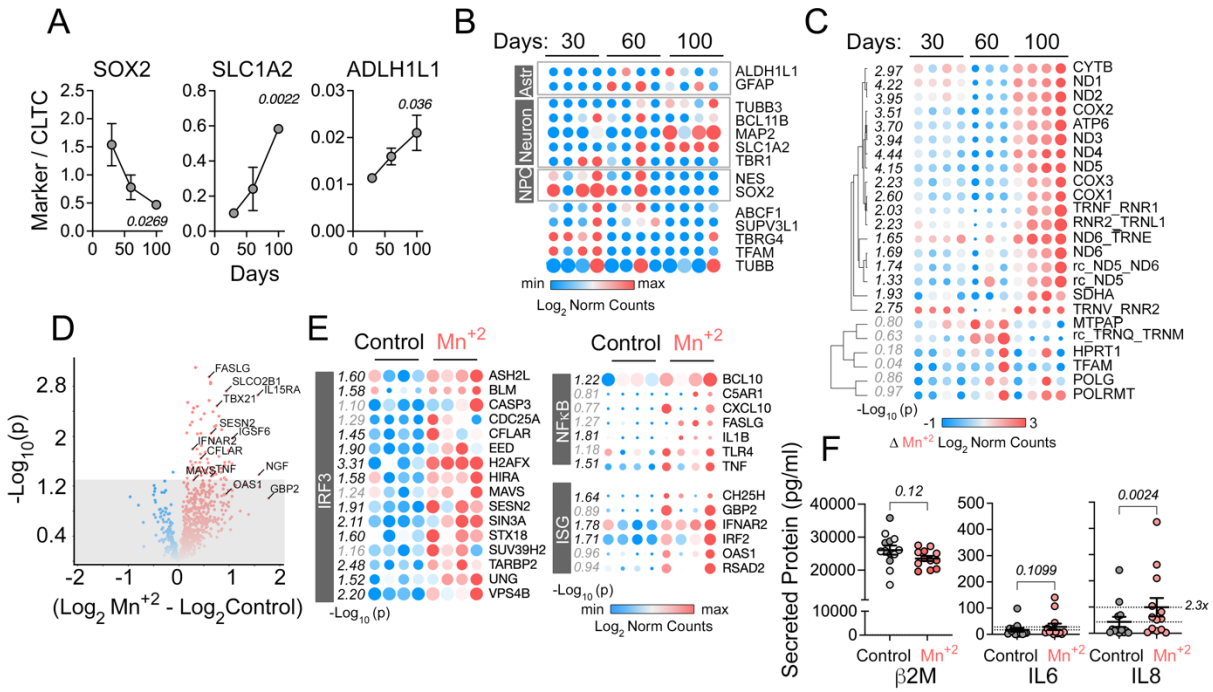

Figure 4: Manganese alters mitochondrial transcripts and induces the interferon type I response in human cerebral organoids.

a) Lineage marker expression measured by NanoString over developmental time (Supplementary Dataset S1). Average ± SEM of 4 organoids per time point. One-way ANOVA followed by Dunnett's multiple comparisons test.

b) Heatmap of RNA levels of organoid differentiation markers and nuclear encoded mitochondrial transcripts measured by NanoString in individual organoids over time of development (Supplementary Dataset S1). Log_2 of normalized counts of the gene were used for the heatmap.

c) Heatmap of nuclear and mitochondrial encoded mitochondrial transcripts measured by NanoString in individual organoids over time of development (Supplementary Dataset S1). The difference of normalized counts from manganese-induced minus non-treated organoids per time point is expressed as Log_2. Non-responsive organelles at 30 days were compared to responses in 100-day organelles. Two-tailed t-test expressed as $-Log_{10}$.

d) Volcano plot of the genes in the Neuroinflammatory panel that change expression in the transcriptome of 100-day organoids following 48h of 250μM manganese treatment (Supplementary Dataset S2). Significance threshold was set at 0.05 (marked by the line).

e) Heatmap of IRF3 or NFκB transcriptional target genes and interferon stimulated genes included in the Neuroinflammatory panel (d) that change following manganese exposure (Supplementary Dataset S2). Two-tailed t-test expressed as $-Log_{10}$.

f) Cytokines in conditioned media collected from 100-day organoids following mock or 48h treatment with 250μM manganese. IL6, IL8 and beta 2 microglobulin levels were determined by MesoScale assay. Average ± SEM. Each dot represents an individual organoid. Data from two organoid batches. Statistics for beta 2 microglobulin paired t test and for IL6 and IL8 Wilcoxon matched-pairs signed rank test.

For b, c and e symbol size is proportional to the Log_2 value in between rows.

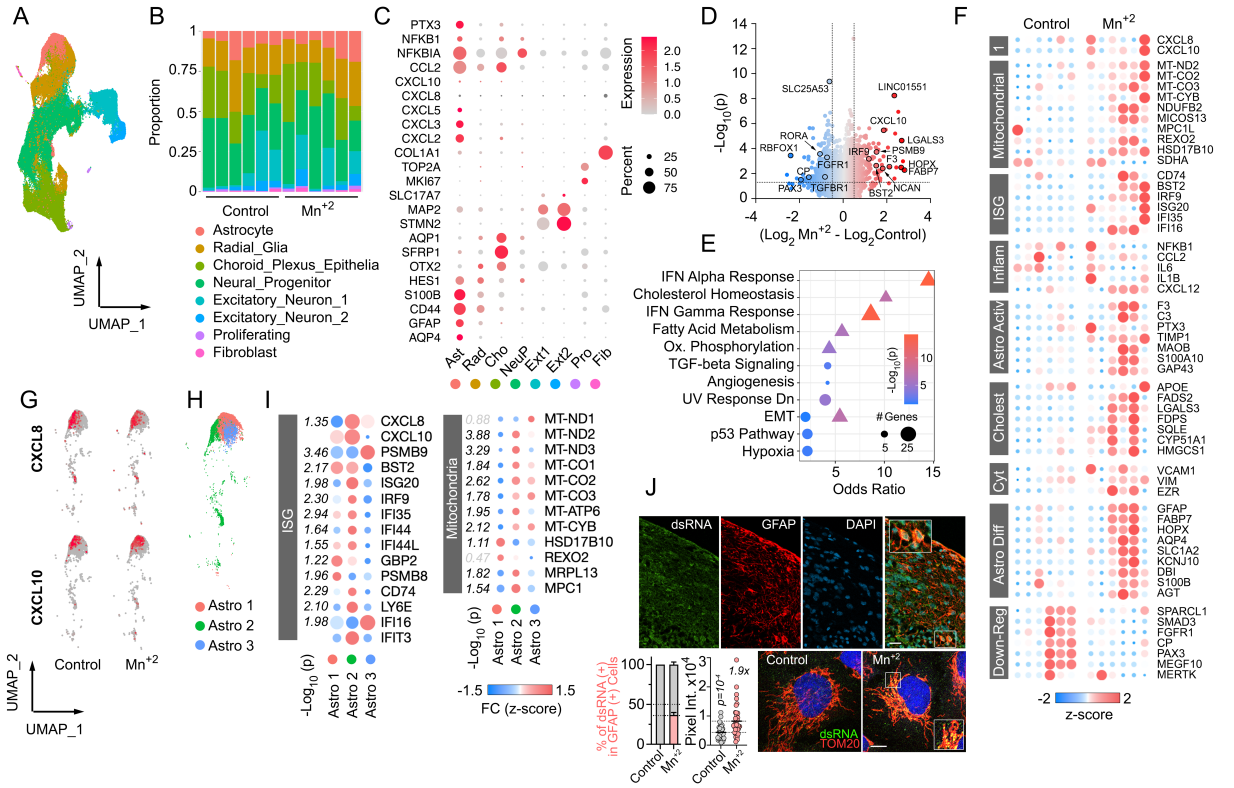

Figure 5: Single cell RNAseq analysis of manganese treated 100-day cerebral organoids.

a) UMAP embedding of all samples (12 organoids aged 100 days) integrated and normalized with SCT transform. Cells are colored by cluster assignment.

b) Proportion of cells assigned to each cluster from individual organoids. Color scheme is the same as in a).

c) Dot plot of cell identity marker and inflammatory gene expression in cell clusters shown in a) (Supplementary Dataset S4). Dot size is proportional to percentage of cells expressing the gene and color reflects average expression level.

d) Volcano plot of the manganese differentially regulated genes in astrocytes (Supplementary Dataset S5). Cut off is p<0.05 and 0.5< average log2FC <-0.5. Highlighted genes belong to the categories identified by gene enrichment analysis (e) or describing astrocyte function.

e) Main up and down regulated pathways in manganese treated astrocytes when comparing the genes curated in Molecular Signatures Database employing EnrichR tool for gene ontology analysis (Supplementary Dataset S6). Triangles are up-regulated genes. Circles are downregulated genes.

f) Heatmap of the scaled gene counts in the astrocyte cluster for individual organoids (Supplementary Dataset S7).

g) Feature plot depicting the cells expressing CXCL8 and CXCL10 in control and manganese treated organoids.

h) UMAP embedding of the subclustered astrocyte population from all organoids.

i) Differential expression of genes belonging to the interferon response, mitochondrial transcripts and RNA processing in the three astrocytes subclusters in response to manganese (Supplementary Dataset S8).

j) Immunofluorescence for dsRNA in manganese treated 100-day organoids and in iPSC derived astrocytes. 1) 100-day organoids stained for GFAP (red), DNA (blue) and dsRNA (green). Scale bar= 25μm. 2) Quantification of the percentage of GFAP cells that were positive for dsRNA in (1) and dsRNA in mitochondria in iPSC derived astrocytes shown in (3).1.9x refers to fold of increase, Mann Whitney test 3) Human astrocytes derived from iPSC treated or not with 250μM Manganese for 24h and stained for dsRNA (green) and the mitochondrial marker TOM20 (red). Scale bar =10μm.

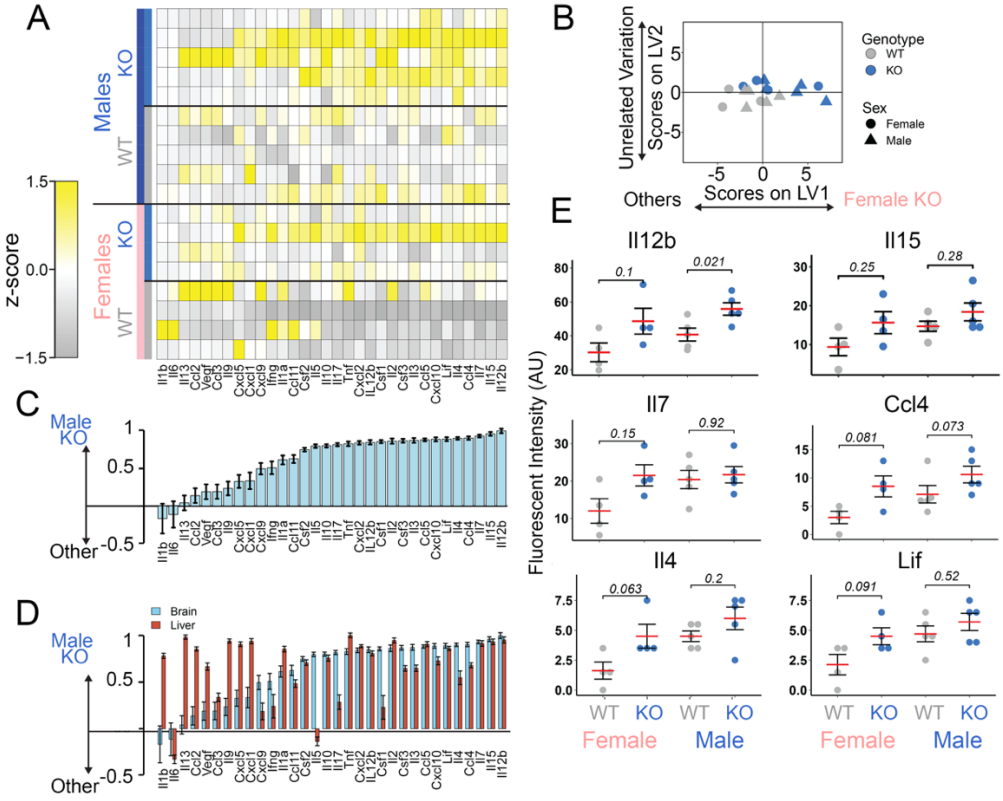

Fig 6: Cortex from a mouse model of hypermanganesemia with dystonia 1 disorder has increased pro-inflammatory cytokines.

a) Heat map of *z*-scored cytokine levels measured by Luminex multiplex assays in cortex samples of wild type and *Slc30a10*$^{-/-}$ male and female mice. The cytokines are named by gene name.

b) A discriminant partial least squares regression model constructed from the cytokine dataset regressed genotype. The model identifies a latent variable (LV1) that scores animals based on cytokine protein expression measurements and predicts genotype. LV2 describes variation that is not connected to genotype. LV1 and LV2 account for approximately 44% and 4% of the dataset variation, respectively.

c) LV1 is composed of cytokines that are elevated and able to predict the KO genotype in a leave-one-out cross validation (mean ± SD across LV1 generated for all models in the cross validation).

d) Comparison of LV1s from cortex and liver (in supplementary data) from *Slc30a10*$^{-/-}$ animals.

e) Example cytokine levels in brain cortex that yielded the highest LV1 scores.